

## COMPUTATIONAL FLUID DYNAMICS MODELLING OF GAS JETS IMPINGING ONTO LIQUID POOLS

Anh NGUYEN and Geoffrey EVANS

Discipline of Chemical Engineering  
 University of Newcastle, Callaghan, 2308, NSW Australia

### ABSTRACT

Gas jets impinging onto a gas-liquid interface of a liquid pool are studied using Computational Fluid Dynamics modelling, which aims to obtain a better understanding of the behaviour of the gas jets used metallurgical engineering industry. The gas and liquid flows are modelled using the Volume of Fluid technique. The governing equations are formulated using the density and viscosity of the “gas-liquid mixture”, which are described in terms of the phase volume fraction. Reynolds averaging is applied to yield a set of Reynolds-averaged conservation equations for the mass and momentum, and the  $k$ - $\varepsilon$  turbulence model. The deformation of the gas-liquid interface is modelled by the pressure jump across the interface via the Laplace equation. The governing equations in the axisymmetric cylindrical coordinates are solved using the commercial CFD code, FLUENT. The computed results are compared with experimental and theoretical data reported in the literature. The CFD modelling allows the simultaneous evaluation of the gas flow field, the free liquid surface and the bulk liquid flow, and provides useful insight to the highly complex, and industrially significant flows in the jetting system.

### NOMENCLATURE

$C$	vertical height from nozzle tip to undisturbed pool free surface	(m)
$D_C$	vessel diameter	(m)
$D_N$	nozzle diameter	(m)
$d_C$	diameter of cavity (see Figure 1)	(m)
$g$	acceleration due to gravity	(m/s <sup>2</sup> )
$H$	vertical height from vessel bottom to undisturbed pool free surface	(m)
$h_C$	depth of cavity measured from free surface (see Figure 1)	(m)
$h_T$	height of dimple measured from free surface (see Figure 1)	(m)
$I$	turbulence intensity	(-)
$K$	coefficient used in Eq. (14)	(-)
$k$	kinetic energy of turbulence	(m <sup>2</sup> /s <sup>2</sup> )
$l$	turbulence length scale	(m)
$M$	jet momentum ( $= \pi \rho_G D_N^2 U_{inlet}^2 / 4$ )	(kgm/s <sup>2</sup> )
$\bar{n}$	surface normal at the interface	(-)
$\bar{n}_w$	unit vector normal to the wall	(-)
$p$	fluid pressure	(kg/ms <sup>2</sup> )
$Re$	flow Reynolds number based on the nozzle aperture and inlet velocity	(-)
$S_\phi$	source term given in Table 1	(-)
$t$	time	(s)
$\bar{t}_w$	unit vector tangential to the wall	(-)
$\mathbf{u}$	velocity	(m/s)
$u$	axial velocity component	(m/s)
$U_{CL}$	centreline axial velocity	(m/s)

$U_{inlet}$	jet inlet velocity	(m/s)
$V$	radial velocity component	(m/s)
$z$	axial coordinate	(m)
$\alpha$	parameter used in Eq. (15)	(-)
$\varepsilon$	energy dissipation rate	(m <sup>2</sup> /s <sup>3</sup> )
$\phi$	“scalar” variable	(-)
$\varphi$	liquid phase volume fraction	(-)
$\varphi_g$	gas phase volume fraction	(-)
$\Gamma_\phi$	diffusion coefficient given in Table 1	(-)
$\mu$	viscosity	(kg/ms)
$\mu_{eff}$	effective viscosity	(kg/ms)
$\mu_t$	turbulent viscosity	(kg/ms)
$\theta$	contact angle	(radians)
$\rho$	density	(kg/m <sup>3</sup> )
$\sigma$	interfacial tension	(kgm <sup>2</sup> /s <sup>2</sup> )

### INTRODUCTION

Gas jets impinging onto a gas-liquid interface of a liquid pool are commonly encountered in the metallurgical industry as a method of agitating a molten liquid phase (e.g. oxygen steel making, vacuum degassing, argon-agitated ladles and top-blown copper converting), and as a method of contacting gas and liquid phases. The gas jet causes a depression to be formed on the liquid surface, and following impingement the gas travels radially outwards from the impact point along the liquid surface thereby dragging the liquid into motion and setting up a recirculation flow within the bulk liquid (see Figure 1).

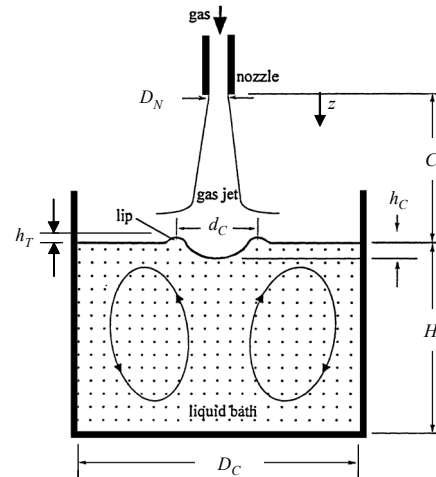
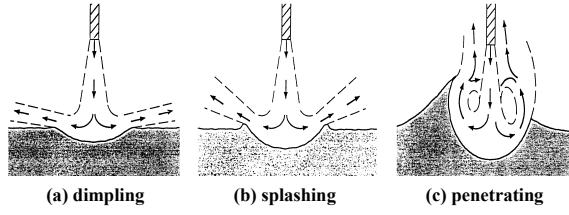


Figure 1: Gas Jet Impinging onto a Liquid Pool

Three different modes of the free surface deformation due to the impinging gas jet have been identified: dimpling, splashing and penetrating, dependent on the jet momentum and the liquid properties (Molloy, 1970). These modes are illustrated in Figure 2. Splashing from the depression, the propagation of surface ripples, oscillation of the depression base and sides, and gas entrainment into the liquid, have

also been observed under certain conditions (Ito et al., 1981). All of these phenomena are of great importance in determining the operating characteristics of an impinging gas jet unit.



**Figure 2:** Modes of Surface Deformation by the Impinging Gas Jet (Molloy, 1970)

The aim of this study is to model a gas jet impinging perpendicularly onto a liquid bath, using CFD, which enables the depression shape, gas and liquid flow characteristics to be determined simultaneously. In particular, the formation of depressions in confined liquid baths is reported and compared to the available experimental and theoretical results from the literature.

## COMPUTATIONAL MODEL

The jetting system is governed by the gas and liquid flows and can be modelled using the volume of fluid (VOF) technique (Hirt and Nichols, 1981), which is a fixed grid technique designed for two or more immiscible fluids where the position of the interface is of interest.

### Mass Conservation, Volume Fraction and Physical Property Equations

In the VOF model the volume fraction of each of the fluids in each computational cell is tracked throughout the computational domain. In addition to the velocity and pressure, the volume fraction is also a variable of the flow field in the VOF technique, and hence is contained in both the mass and momentum equations. For example, the continuity equation for the liquid phase with a volume fraction,  $\phi$ , has the following form:

$$\frac{\partial \phi}{\partial t} + \mathbf{u} \cdot \text{div} \phi = 0 \quad (1)$$

where  $t$  and  $\mathbf{u}$  are velocity and time, respectively. A similar expression is used for the gas phase, where the gas volume fraction,  $\phi_g$ , is given by:

$$\phi_g = 1 - \phi \quad (2)$$

Clearly, in each control volume the volume fractions of all phases must sum to unity. Therefore, if the control volume is full of liquid then  $\phi = 1$ . Similarly, if there is no liquid in the volume, i.e. it is full of gas, then  $\phi = 0$ . The volume fraction for each of the phases is used to determine volume-averaged values for variables and fluid physical properties. For example, the density  $\rho$  and viscosity  $\mu$  of each control volume within the domain are determined by the composite expressions as follows:

$$\rho = \rho_g(1 - \phi) + \rho_l \phi \quad (3)$$

$$\mu = \mu_g(1 - \phi) + \mu_l \phi \quad (4)$$

### Momentum Conservation Equation

The momentum equation for the computational domain in its generalised form can be written as:

$$\frac{\partial}{\partial t}(\rho \mathbf{u}) + \text{div}(\rho \mathbf{u}) = -\text{grad}(p) + \text{div}[\mu \text{grad}(\mathbf{u})] + \rho \mathbf{g} \quad (5)$$

where  $\mathbf{g}$  is the acceleration due to gravity,  $p$  is the fluid pressure, and  $\rho$  and  $\mu$  are density and viscosity, based on Eqs. (3) and (4), respectively.

### Turbulent Flow Equations

Since the liquid and the gas velocities exiting the nozzles are relatively high, it is appropriate to simulate the flow in the jetting system using a turbulent flow model. To do this, the flow variables, such as  $\phi$ , are decomposed into mean,  $\bar{\phi}$ , and fluctuating,  $\phi'$ , components in the standard way, such that:  $\phi = \bar{\phi} + \phi'$ . Inserting the decomposed variables into instantaneous equations given in the previous equations, and applying Reynolds averaging, yield a set of Reynolds-averaged conservation equations for the mass and momentum, as well as the kinetic energy,  $k$ , of turbulence, and its dissipation rate,  $\varepsilon$ . For later convenience and dropping the overbar on the mean variables the Reynolds-averaged equation can be written in the following generic transport equation form:

$$\frac{\partial(\rho \phi)}{\partial t} + \text{div}(\rho \mathbf{u} \phi) = \text{div}(\Gamma_\phi \text{grad} \phi) + S_\phi \quad (6)$$

or in axisymmetric cylindrical coordinates this can be written as

$$\frac{\partial(\rho \phi)}{\partial t} + \frac{1}{r} \left[ \frac{\partial(r \rho U \phi)}{\partial z} + \frac{\partial(r \rho V \phi)}{\partial r} \right] = \frac{1}{r} \left[ \frac{\partial}{\partial z} \left( r \Gamma_\phi \frac{\partial \phi}{\partial z} \right) + \frac{\partial}{\partial r} \left( r \Gamma_\phi \frac{\partial \phi}{\partial r} \right) \right] + S_\phi \quad (7)$$

where the ‘‘scalar’’ variable  $\phi$ , the diffusion coefficient  $\Gamma_\phi$  and source term  $S_\phi$  in the respective governing equation are given in Table 1.

Eq.	$\phi$	$\Gamma_\phi$	$S_\phi$
Cont.	$\phi / \rho$	0	0
r-Mom.	$V$	$\mu_{\text{eff}}$	$-\frac{\partial p}{\partial r} + \frac{\partial}{\partial z} \left( \mu_{\text{eff}} \frac{\partial U}{\partial r} \right) + \frac{1}{r} \frac{\partial}{\partial r} \left( r \mu_{\text{eff}} \frac{\partial V}{\partial r} \right) - \frac{2\mu_{\text{eff}} V}{r^2}$
z-Mom.	$U$	$\mu_{\text{eff}}$	$-\frac{\partial p}{\partial z} + \frac{\partial}{\partial z} \left( \mu_{\text{eff}} \frac{\partial U}{\partial z} \right) + \frac{1}{r} \frac{\partial}{\partial r} \left( r \mu_{\text{eff}} \frac{\partial V}{\partial z} \right) + g$
k-eq.	$k$	$\mu + \frac{\mu_t}{\sigma_k}$	$\mu_t \left[ \left( \frac{\partial U}{\partial r} + \frac{\partial V}{\partial z} \right)^2 + 2 \left( \frac{\partial U}{\partial z} \right)^2 \right] + 2 \left( \frac{\partial V}{\partial r} \right)^2 + 2 \left( \frac{V}{r} \right)^2 - \rho \varepsilon$
$\varepsilon$ -eq.	$\varepsilon$	$\mu + \frac{\mu_t}{\sigma_k}$	$C_1 \frac{\varepsilon}{k} \mu_t \left[ \left( \frac{\partial U}{\partial r} + \frac{\partial V}{\partial z} \right)^2 + 2 \left( \frac{\partial U}{\partial z} \right)^2 \right] + 2 \left( \frac{\partial V}{\partial r} \right)^2 + 2 \left( \frac{V}{r} \right)^2 - C_2 \rho \frac{\varepsilon^2}{k}$

$\mu_t = C_\mu \rho k^2 / \varepsilon$  (= turbulent viscosity);

$\mu_{\text{eff}} = \mu + \mu_t$  (= effective viscosity), and

$C_\mu = 0.09$ ;  $C_1 = 1.44$ ;  $C_2 = 1.92$ ;  $\sigma_k = 1.0$ ;  $\sigma_\varepsilon = 1.3$

**Table 1:** Diffusion Coefficients and Source Terms in the Generic Transport Eq. (7)

In the case of turbulence quantities, a single set of transport equations is solved, and the variables  $k$  and  $\varepsilon$  or the Reynolds stresses are shared by the phases throughout the field. In the governing equations in Table 1, the effect of turbulence is incorporated through the “Reynolds stresses”, which are related to the mean flow variables via the standard  $k$ - $\varepsilon$  model of turbulence (Launder and Spalding, 1972). The  $k$ - $\varepsilon$  model belongs to the class of the two-equation turbulence models and is widely used for practical engineering flow calculations. The model is semi-empirical and is appropriate for high Reynolds number flows, such as those for the jetting system.

## COMPUTATIONAL MODEL PARAMETERS

The computational modelling was carried out using the FLUENT CFD code based on the volume of fluid (VOF) technique, and applying the  $k$ - $\varepsilon$  two-equation, with the standard wall function, to describe the turbulence.

### Geometry and Grid Arrangement

The geometry and computational domain used to model the jetting system are shown in Figure 3(a). Only a 2D axisymmetric computational domain was considered, and meshed non-uniformly by the rectangular scheme (Figure 3(b)). Strong grid clustering was used along the centreline of the gas jet direction. Grid contraction toward the free surface (described by line BE in Figure 3(b)) was required for capturing the gas and liquid flows, and the deformation of the gas-liquid interface.

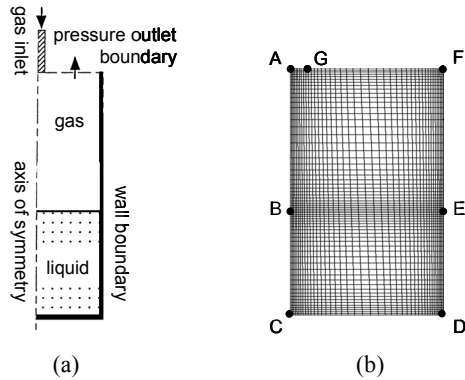


**Figure 3:** Computational Domain and Grid Arrangement for Axisymmetric Impinging Gas Jet.

### Boundary Conditions

Five types of boundary conditions were used to describe the flow field within the computational domain:

**Gas Jet Inlet:** The condition in the nozzle (boundary AG in Figure 3(b)) is important in predicting the centreline velocity and shear stress. The velocity profile at the nozzle exit is affected by the nozzle design such as the length-to-diameter ratio and nozzle shape. In this paper, a uniform nozzle velocity profile was considered. The VELOCITY-INLET boundary conditions imposed at the nozzle are described by

$$U = U_{inlet} \text{ and } V = 0 \quad (8)$$

$$k = k_{inlet} = 1.5(U_{inlet}I)^2 \quad (9)$$

$$\varepsilon = \varepsilon_{inlet} = (C_{\mu})^{3/4} (k_{inlet})^{3/2} / l \quad (10)$$

where the turbulence length scale,  $l$ , at the inlet is assumed to be the nozzle aperture. Turbulence intensity,  $I$ , at the inlet is estimated using the turbulent fluctuating to mean velocity at inlet by  $I = u'/U_{inlet} \cong 0.16 (Re)^{-1/8}$ , where  $Re$  is the flow Reynolds number based on the nozzle aperture and inlet velocity.

**Solid Boundaries (the wall surface):** The wall boundary conditions CD, DE and EF (Figure 3(b)) were used at the solid wall of the liquid pool where the no-slip boundary conditions were imposed. For large (unconfined) pools, the deformation of the free surface is not significantly affected by the pool dimensions, the precise location of point F is not important. In this case, the length of section EF was chosen as being two-thirds of AB. In the simulations with confined pools, point F was located at the top right hand corner of the computational domain.

For the evaluation of the wall effect on turbulence, the wall-function and near-wall-modelling (Launder and Spalding, 1974) approaches have been used to model the wall-bounded turbulent flows. In the former, semi-empirical formulas are used to bridge the viscosity-affected region (viscous sublayer and buffer layer) between the wall and the fully turbulent region. The mesh is not resolved. In the second approach, the turbulence models are modified to enable the viscosity-affected region to be resolved with a mesh all the way to the wall. No wall function is used. However, a large number of cells are required in the near-wall-modelling approach.

Both approaches were initially tested in our transient simulations which showed no significant difference in the flow patterns. Therefore, the wall-function approach which is computationally economical, robust was used in our calculation. In this model the turbulent kinetic energy varies in a parabolic shape within the viscous sublayer, which corresponds to the linear variation of a fluctuating velocity with distance from the wall, and then linearly over the remainder of the cell. Unlike the turbulent kinetic energy, the shear stress is zero within the viscous sublayer, but undergoes an abrupt increase at the boundary, before varying linearly toward the outer region of the cell. The treatment of evaluating mean generation and destruction rates is also incorporated in the  $\varepsilon$ -equation.

**Gas Exit Boundary:** The boundary FG in Figure 3(b) is the gas exit boundary. The OUTFLOW (fully developed) boundary conditions were first used at this boundary. Under the OUTFLOW boundary conditions the velocity gradients across the boundary are set to zero. However, it was found that reversed flows occurred at these boundaries, indicating that the fluid motion was not fully developed. Consequently, the PRESSURE outlet boundary condition was used. The PRESSURE outlet conditions require a numerical value for the relative static (gauge) pressure at the outlet boundary. This value was set to zero, i.e. assumed to be at atmospheric pressure. All other conditions associated with velocities at the PRESSURE outlet boundaries were extrapolated from the interior of the computational domain.

**Axis of Symmetry:** The axis boundary was used along centrelines AB and BC. The radial velocity component  $V$  and the gradients of the other dependent variables were equal to zero.

**Gas-Liquid Interface:** The deformation of the gas-liquid interface (described by line EB in Figure 3(b)) was coupled by the pressure jump across the interface via the Laplace equation, i.e.

$$p_l - p_g = \sigma \operatorname{div}(\bar{\mathbf{n}}/|\bar{\mathbf{n}}|) \quad (11)$$

where  $p_l$  and  $p_g$  are the pressures in the two fluids on either side of the interface, and  $\sigma$  is the interfacial tension. The bracketed term on the right hand side describes the local interface curvature, which is defined in terms of the divergence of the unit normal  $\bar{\mathbf{n}}/|\bar{\mathbf{n}}|$ , where  $\bar{\mathbf{n}}$  is the surface normal at the interface and is related to the volume fraction of the liquid phase by:

$$\bar{\mathbf{n}} = \operatorname{grad}(\varphi) \quad (12)$$

At the wall, the surface normal at the live cell next to the wall is defined in terms of the contact angle,  $\theta$ , between the interface and the wall by:

$$\bar{\mathbf{n}} = \bar{\mathbf{n}}_w \cos \theta + \bar{\mathbf{t}}_w \sin \theta \quad (13)$$

where  $\bar{\mathbf{n}}_w$  and  $\bar{\mathbf{t}}_w$  are the unit vectors normal and tangential to the wall, respectively. The combination of the contact angle with the normally-calculated surface normal one cell away from the wall determines the local curvature of the surface. All the results reported in this paper were obtained with the contact angle of 90 degrees.

#### Modelling Parameters

Numerical values for the major parameters used in a number of the numerical computational simulations are given in Table 2.

Run	$D_N$ (mm)	$D_C$ (mm)	$C$ (mm)	$H$ (mm)	$U_{inlet}$ (m/s)
1	6	290	154	111	56.2
2	11	300	220	1500	100
3	11	200	220	1000	100
4	11	100	220	500	100

**Table 2:** Summary of the Simulation Conditions

Parameters of Run 1 were selected according to a similar experimental system (Zhang et al., 1985). Runs 2-4 were used to investigate the influence of the diameter of the confined liquid pools on the deformation of the gas-liquid interface. All the numerical simulations were carried out for air-water systems at ambient pressure and temperature.

#### Numerical Procedure and Computational Methodology

The governing differential transport equations were converted to algebraic equations before being solved numerically. The finite volume scheme (Fletcher, 1998), which involves integrating the governing equations about each control volume, yielding discrete equations that conserve each quantity on a control-volume basis, was applied to Eq. (7). The governing equations were discretised using the second-order upwind scheme to achieve the best accuracy. The interpolation of the pressure values at the cell faces, using the momentum equation, was carried out using the PRESTO (PREssure STaggering Option) scheme, which improved the convergence rate and the stability of the computation. This interpolation scheme uses the discrete continuity balance for a “staggered” control volume about the face to compute the “staggered” (face) pressure and is similar in spirit to the staggered-grid

schemes used with structured meshes (Patankar, 1980). Pressure-velocity coupling was achieved by using the PISO (Pressure-Implicit with Splitting of Operators) algorithm (Versteeg and Malalasekera, 1995) with neighbour correction, which is highly recommended for both steady state and transient calculations on meshes with a degree of distortion. The governing equations were solved sequentially using the commercial FLUENT code.

## RESULTS AND DISCUSSION

In general, the transient solutions reach steady state relatively fast, within 10 seconds. In particular, the deformed shape of the gas-liquid is stable within the first second. The circulation of the liquid in the pool usually takes some time to reach the steady state condition. In the following, steady state solutions are reported.

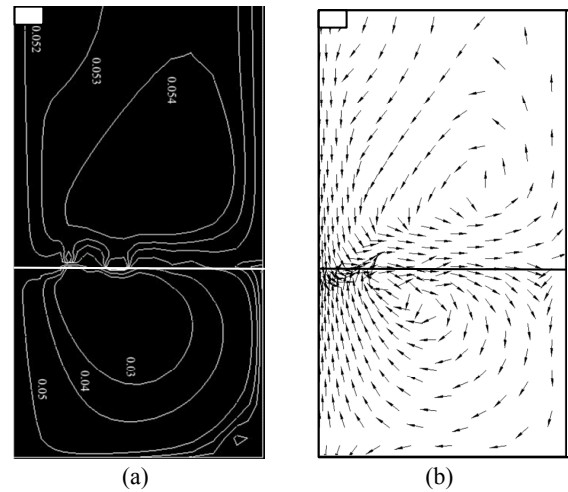


**Figure 4:** Stream Function (a) and Velocity (b) for Run 1

Figure 4(a) shows the stream function contours for Run 1. The computed field is similar to the experimental streamline pattern available in the literature (Zhang et al., 1985) when the system is agitated by an impinging jet and by a submerged gas stream. Since the submerged gas stream is not considered here, the centre of the circulating flow in the liquid phase is close to the centreline. The directional<sup>1</sup> field for the velocity of both the gas and liquid flows is shown in Figure 4(b). Again, the computed velocity field qualitatively agrees with the experimental measurements available in the literature (Zhang et al., 1985) in that liquid in the pool moves towards the centreline and upwards to the gas-liquid interface, leading to the mixing in the pool.



**Figure 5:** Gas-Liquid Interface Profile for Run 1

<sup>1</sup> Magnitude of the arrows is fixed and show direction of the flow only.

The shape of the gas-liquid interface for Run 1 is shown in Figure 5, and corresponds to the dimpling mode illustrated in Figure 1. The profile is also consistent with the gas flow velocity field shown in Figure 4(b). It is further evident from the figure that part of the gas-liquid interface close to the centreline is not smooth, probably due to strong turbulence of the gas phase flow in this region.

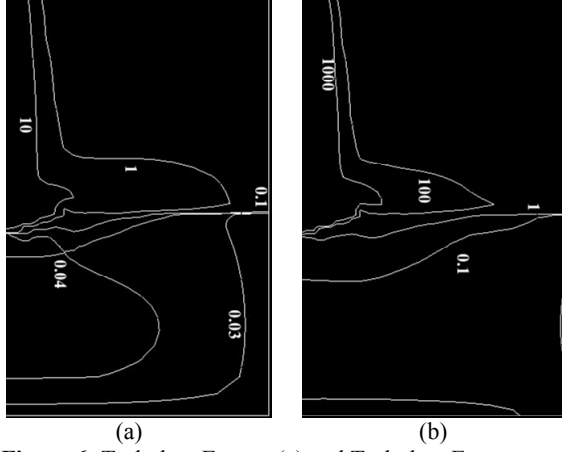


**Figure 6:** Turbulent Energy (a) and Turbulent Energy Dissipation Rate (b) for Run 1

The distribution of the turbulent energy and its dissipation rate are shown in Figures 6(a) and 6(b), respectively. As expected, high values of both these quantities can be seen in the region close to the gas-liquid interface where intensive mixing and mass transfer can occur.

Quantitative examination of the computed gas-liquid interface profile given in Figure 5 found that the depth,  $h_C$ , of the cavity and height,  $h_T$ , of the dimple (all measured from the free surface – see Figure 1) were 12 and 2 mm, respectively. The computed depth compared favourably with the theoretical prediction<sup>2</sup> of 13 mm, based on stagnation pressure analysis for an unconfined jet (Banks and Chandrasekhara, 1963; Banks and Chandrasekhara, 1965):

$$\frac{h_C}{C} \left( 1 + \frac{h_C}{C} \right)^2 = \frac{2K^2}{\pi} \left( \frac{M}{\rho_L g C^3} \right), \quad (14)$$

where  $M$  is the jet momentum and  $K$  is a coefficient which is a function of the jet Reynolds number. A value of 7.6 was chosen for  $K$  (Wakelin, 1966).

The computed width,  $d_C$ , of the cavity (obtained from Figure 5) of 61 mm also compares favourably with a predicted value 59 mm, which is based on the mass of displaced liquid and assuming a 4<sup>th</sup> order polynomial cavity profile. The resultant expression is reported by Forrester and Evans (1996) as:

$$d_C = (h_C + h_T) \sqrt{\frac{12(1+\alpha)}{\pi}} \sqrt{\frac{M}{\rho_L g (h_C + h_T) h_C^2}}, \quad (15)$$

where  $\alpha$  is a parameter with a value of 0 for shallow cavities, while is equal to 1 for deeper cavities. For the case of Run 1 and  $\alpha=0$  was assumed.

<sup>2</sup> The analysis does not account for the formation of the dimple at the edge of the cavity, i.e.  $h_T=0$ .

The simulations of Runs 2-4 aimed to investigate the effect of the nozzle-to-pool diameter ratio on the deformation of the gas-liquid interface. The nozzle, jet velocity, and nozzle clearance were kept constant while the pool diameter was varied from 300 to 100 mm in order to provide the full range of unconfined, through to confined deformation of the gas-liquid interface. The liquid depth was kept constant at 5 times the pool diameter in order that the deformation was not affected by the base of the pool. The nozzle-interface clearance was maintained at 20 times the nozzle diameter so that a “free” turbulent jet could interact with the free surface. The jet velocity of 100 m/s produced a jet momentum of about 1.1 N.

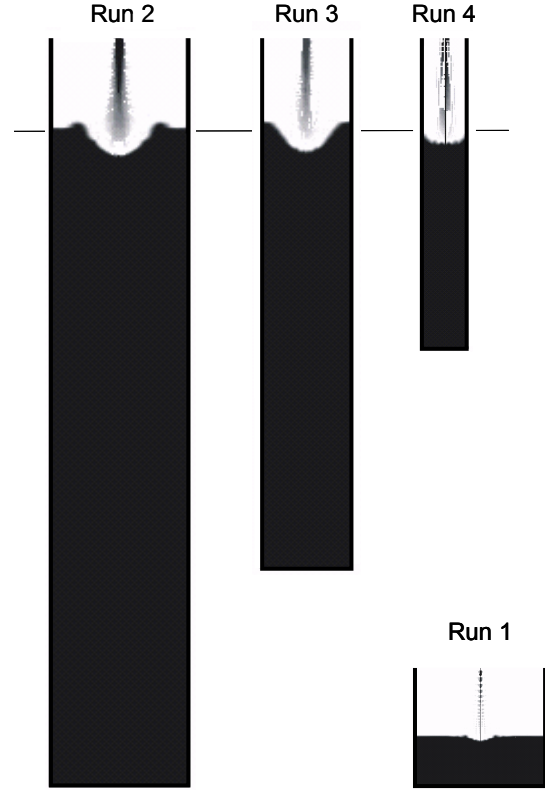


**Figure 7:** Gas-Liquid Interface Profiles for Runs 1-4

The simulated profiles are presented in Figure 7. It can be seen that the cavity shape for Run 2 is similar to that of the unconfined jet case in Run 1, where the outer boundary of the cavity exhibits a raised dimple and beyond this region the free surface is flat (undisturbed). The cavity for Run 3 has similar profile to Run 2, except that there is flat free surface beyond the cavity boundary. Run 3 could be either just at the limit of the unconfined jet case or actually be confined. Run 4 is clearly a confined system, where the cavity diameter,  $d_C$ , is equal to vessel diameter,  $D_C$ ; and the cavity depth is given by (Forrester and Evans, 1996):

$$h_C = \left( \frac{24\sqrt{3}(1+\alpha)}{\pi(7-3)\sqrt{3}} \right) \left( \frac{M}{\rho_L g D_C^2} \right). \quad (16)$$

The simulated and predicted cavity dimensions are summarised in Table 2. Also included are the assumed  $\alpha$  and  $K$  values used to obtain the model predictions. A shallow cavity ( $\alpha=0$ ) was assumed for Run 1 only; for Runs 2-4,  $\alpha$  was set to 1. Moreover, Runs 1-3 were assumed to be unconfined, with Run 4 being the only confined system. It can be seen from the results that the

cavity dimension obtained from the CFD simulations were reasonably consistent with the theoretical predictions, even including Run 3 where it was not clear if the system was confined or unconfined. This result suggests that the free surface can be modelled as an unconfined system up to the point where the cavity boundary actually reaches the vessel wall. For the confined jet case (Run 4) the CFD prediction for the cavity depth is much less than the theoretical value. The reason for this can be found by comparing the interface height relative to the undisturbed liquid height (ULH) in the vessel (shown as a horizontal line). For Run 4, no part of the disturbed interface is above the UDL, and consequently some of the liquid must have been removed from the vessel as a result of splashing. The use of the Pressure outlet for the gas exits GF boundary conditions in the VOF method allows the removal of water (splashing) from the vessel when it reaches the boundary.

Run	CFD			Theory				
	$h_C$	$h_T$	$d_C$	$K$	$\alpha$	$h_C$	$h_T$	$d_C$
1	12	2	61	7.6	0	14 <sup>a</sup>	0	56 <sup>b</sup>
2	64	14	146	8.8	1	66 <sup>a</sup>	0	123 <sup>b</sup>
3	64	12	119	8.8	1	66 <sup>a</sup>	0	122 <sup>b</sup>
4	27	—	100	8.8	1	159 <sup>c</sup>	80 <sup>d</sup>	100 <sup>e</sup>

Unconfined: <sup>a</sup> Eq. (14); <sup>b</sup> Eq. (15).  
 Confined: <sup>c</sup> Eq. (14); <sup>d</sup>  $h_T=0.5h_C$ ; <sup>e</sup>  $d_C=D$ .

**Table 3:** CFD and Theoretical Cavity Dimensions

From the information given in Table 3 it can be seen that a value of  $K=7.6$  was assumed for Run 1, while a value of 8.8 was chosen for Runs 2-4. The numerical value of  $K$  is a function of the jet Reynolds number (Wakelin, 1966), and can be related to the decay in the centreline gas jet velocity,  $U_{CL}(z)$ , as a function of distance,  $z$ , from the nozzle outlet (see Fig. 1) by the expression:

$$\frac{U_{CL}(z)}{U_{inlet}} = \frac{K}{z/D_N + K} \quad (17)$$

Equation (17) is based on the original theoretical modelling of (Banks and Chandrasekhara, 1963), but has been modified to account for the apparent absence of a potential core immediately downstream of the nozzle exit.

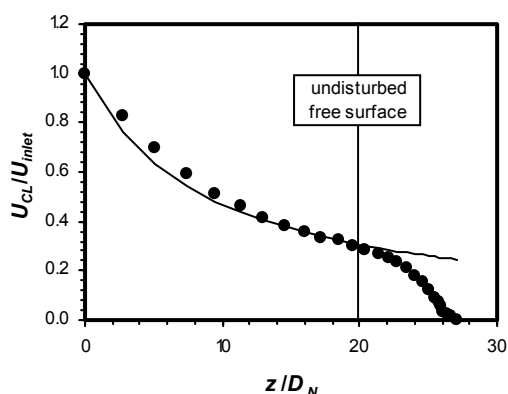


**Figure 8:** Centreline Gas Jet Velocity for Run 2  
 [● CFD results, — Eq. (17) with  $K=8.8$ ]

A comparison between CFD modelling (closed circles) and prediction from Eq. (17), for  $K=8.8$ , is shown in Figure 8. It can be seen that the hyperbolic dependence of the centreline velocity agrees with the CFD modelling up to the point at which the jet enters the cavity region.

## CONCLUSIONS

Computational Fluid Dynamics modelling was used to study gas jets impinging onto a gas-liquid interface of a liquid pool. The gas and liquid flows were modelled using the Volume of Fluid technique. The phase volume fraction was used to describe the density and viscosity of the phases involved. The governing equations were formulated using Reynolds averaging for the mass and momentum. Turbulence was modelled using the  $k-\varepsilon$  turbulence model. The deformation of the gas-liquid interface is modelled using the Laplace equation for the pressure jump across the interface. The governing equations in the axisymmetric cylindrical coordinates are solved using the commercial CFD code, FLUENT. The computed results are compared with experimental and theoretical data reported in the literature. The CFD modelling allows the simultaneous evaluation of the gas flow field, the free liquid surface and the bulk liquid flow, and provides useful insight to the highly complex, and industrially significant flows in the jetting system.

## REFERENCES

- BANKS, R.B. and CHANDRASEKHARA, D.V., 1963. Experimental Investigation of the Penetration of a High-Velocity Gas Jet Through a Liquid Surface. *J. Fluid Mech.*, 15: 13-34.
- BANKS, R.B. and CHANDRASEKHARA, D.V., 1965. Experimental study on the Impingement of a liquid jet on the Surface of a Heavier Liquid. *J. Fluid Mech.*, 23: 229-240.
- FLETCHER, C.A.J., 1998. *Computational Techniques for Fluid Dynamics 1. Fundamental and General Techniques*, 1. Springer-Verlag, Berlin.
- FORRESTER, S.E. and EVANS, G.M., 1996. Air Jets Impinging onto Unconfined and Confined Liquid Pools. 3rd CFX International Users Conference, Harwell, UK, 195.
- HIRT, C.W. and NICHOLS, B.D., 1981. Volume of Fluid (VOF) Method for the Dynamics of Free Boundaries. *J. Comput. Phys.*, 39: 201-225.
- ITO, R., HIRATA, Y., MA, Y. and YOSHIDA, F., 1981. Velocity of a Liquid Surface on which an Air Jet is Impinging. *Int. Chem. Engng*, 21: 259-268.
- LAUNDER, B.E. and SPALDING, D.B., 1972. *Mathematical Models of Turbulence*. Academic, London, 169 pp.
- LAUNDER, B.E. and SPALDING, D.B., 1974. *The Numerical Computation of Turbulent Flows*. Computer Methods in Applied Mechanics and Engineering, 3: 269-287.
- MOLLOY, N.A., 1970. Impinging Jet Flow in a Two-Phase System: The Basic Flow Pattern. *J. Iron Steel Inst.*, October: 943-950.
- PATANKAR, S.V., 1980. *Numerical Heat Transfer and Fluid Flow*. Hemisphere, Washington, D.C.
- WAKELIN, D.H., *The Interaction Between Gas Jets and the Surface of Liquids Including Molten Metals*. PhD Thesis, University of London, UK.
- VERSTEEG, H.K. and MALALASEKERA, W., 1995. *An Introduction to Computational Fluid Dynamics: The Finite Volume Method*. Addison-Wesley, Edinburgh, 257 pp.
- ZHANG, J., DU, S. and WEI, S., 1985. Flow Field in a Bath Agitated by Symmetrically Placed Impinging Gas Jet and Submerged Gas Stream. *Ironmaking and Steelmaking*, 12: 249-255.